High-frequency dynamic nuclear polarization using biradicals: A multifrequency EPR lineshape analysis

Kan-Nian Hu,[1,2] Changsik Song,[2] Hsiao-hua Yu,[2] Timothy M. Swager,[2] and Robert G. Griffin[1,2,a)]

[1]*Francis Bitter Magnet Laboratory, Massachusetts Institute of Technology, Cambridge, Massachusetts 02139, USA*

[2]*Department of Chemistry, Massachusetts Institute of Technology, Cambridge, Massachusetts 02139, USA*

(Received 30 April 2007; accepted 29 October 2007; published online 23 January 2008)

To date, the cross effect (CE) and thermal mixing (TM) mechanisms have consistently provided the largest enhancements in dynamic nuclear polarization (DNP) experiments performed at high magnetic fields. Both involve a three-spin electron-electron-nucleus process whose efficiency depends primarily on two electron-electron interactions—the interelectron distance R and the correct electron paramagnetic resonance (EPR) frequency separation that matches the nuclear Larmor frequency, $|\omega_{e2}-\omega_{e1}|=\omega_n$. Biradicals, for example, two 2,2,6,6-tetramethyl-piperidine-1-oxyls (TEMPOs) tethered with a molecular linker, can in principle constrain both the distance and relative g-tensor orientation between two unpaired electrons, allowing these two spectral parameters to be optimized for the CE and TM. To verify this hypothesis, we synthesized a series of biradicals—bis-TEMPO tethered by n ethylene glycol units (a.k.a. BTnE)—that show an increasing DNP enhancement with a decreasing tether length. Specifically at 90 K and 5 T, the enhancement grew from ~40 observed with 10 mM monomeric TEMPO, where the average $R\sim 56$ Å corresponding to electron-electron dipolar coupling constant $\omega_d/2\pi=0.3$ MHz, to ~175 with 5 mM BT2E (10 mM electrons) which has $R\sim 13$ Å with $\omega_d/2\pi=24$ MHz. In addition, we compared these DNP enhancements with those from three biradicals having shorter and more rigid tethers—bis-TEMPO tethered by oxalyl amide, bis-TEMPO tethered by the urea structure, and 1-(TEMPO-4-oxyl)-3-(TEMPO-4-amino)-propan-2-ol (TOTAPOL) TOTAPOL is of particular interest since it is soluble in aqueous media and compatible with DNP experiments on biological systems such as membrane and amyloid proteins. The interelectron distances and relative g-tensor orientations of all of these biradicals were characterized with an analysis of their 9 and 140 GHz continuous-wave EPR lineshapes. The results show that the largest DNP enhancements are observed with BT2E and TOTAPOL that have shorter tethers and the two TEMPO moieties are oriented so as to satisfy the matching condition for the CE. © *2008 American Institute of Physics*.
[DOI: 10.1063/1.2816783]

I. INTRODUCTION

The last decade has witnessed the appearance of a number of new solid-state nuclear magnetic resonance (SSNMR) magic angle spinning (MAS) techniques that are capable of providing spectral assignments and highly accurate bond distances[1–8] and torsion angles,[9–13] and the development of these methods continues at a rapid pace. Consequently, MAS experiments have emerged as an important tool in structural studies of membrane[14] and amyloid[8,9,13,15–19] peptides and proteins, systems where conventional diffraction and liquid-state NMR structural techniques have had limited success. However, despite the promise of the SSNMR techniques, their applicability remains limited by the intrinsic low sensitivity of the methods. Thus, if multidimensional MAS experiments are to be generally useful, then it is essential to rectify this deficiency.

Microwave driven dynamic nuclear polarization (DNP) can be used in conjunction with MAS to enhance NMR signal-to-noise ratios by two to three orders of magnitude.[20–28] The enhanced intensity of the NMR signals arises from the transfer of electron spin polarization from either endogenous or exogenous unpaired electrons to the nuclear spin system.[20] However, the ever-increasing magnetic fields employed in contemporary multidimensional NMR experiments present new challenges that must be addressed for DNP to be effectively integrated into MAS experiments.

First, it has been necessary to develop high power (>10 W), high-frequency (100–600 GHz) microwave sources to excite the electron paramagnetic resonance (EPR) transitions that in high fields lie in the subterahertz (140–600 GHz) regime.[26,29–33] Second, DNP experiments are most efficient when performed at low temperatures (<90 K) and therefore, MAS probes capable of low-temperature, quadruple resonance (^{1}H, ^{13}C, ^{15}N, and e^-) experiments are required. Finally, efficient polarizing agents

a)Electronic mail: rgg@mit.edu.

must be developed that support the TM and CE mechanisms that are established to yield the optimal enhancements in high-field DNP experiments. In the past, polarizing agents for DNP experiments consist of monomeric paramagnetic centers—free radicals such as 2,2,6,6-tetramethyl-piperidine-l-oxyl (TEMPO) or α,γ-bisdiphenylene-β-phenylallyl[24] or metal ions such as Cr^{5+} (Ref. 34)—dispersed in glassy media. However, with these polarizing agents, there exists a significant discrepancy between measurable DNP enhancement factors and the theoretical maximum, given by $\sim(\gamma_e/\gamma_n)$, where γ_e and γ_n are electron and nuclear gyromagnetic ratios, respectively (e.g., ~660 for the ^{1}H polarization). Consequently, improving DNP enhancements via the design of new polarizing agents is a third avenue relevant to the improvement of high-field DNP experiments and the subject of this paper.

Polarizing mechanisms involved during continuous microwave irradiation at or near the electron Larmor frequency ω_c include the Overhauser effect (OE), solid effect (SE), cross effect (CE), and thermal mixing (TM).[20,35] The origin of the OE is the electron-nuclear cross relaxation arising from stochastic electron-nuclear interactions with a correlation time τ_c. However, high magnetic fields diminish the importance of the OE because as ω_e increases, it becomes increasingly difficult to fulfill the constraint $\omega_e\tau_c<1$. Only when this inequality is satisfied is there significant spectra density from the rotation and translational motion for the OE to be an important polarization mechanism. Thus, with the exception of the special case of liquid-state DNP experiments based on scalar interactions involving transient molecular contacts,[36] the most generally successful approach to enhancing polarization of nuclei in a liquid at high fields presently relies on polarization in the solid state followed by a rapid melting.[28]

DNP of nuclear spins in solid dielectrics occurs through the SE, CE, or TM mechanisms and depends on the relationship between the nuclear Larmor frequency ω_n and linewidth δ of the EPR spectrum of the paramagnetic species involved. In powder systems with randomly oriented paramagnetic species, the SE is the dominant DNP mechanism when $\delta<\omega_n$, whereas the CE and TM prevail for the condition $\delta>\omega_n$. Further, DNP enhancements arising from the SE scale as ω_n^{-2}, whereas enhancements from the CE and TM scale as ω_n^{-1}, and therefore, the CE and TM are the more efficient mechanisms for high-field DNP and both are present when the TEMPO radical is the polarizing agent. Note that at high field, TEMPO exhibits an inhomogeneously broadened EPR lineshape with $\delta>\omega_n$ that arises from g-value anisotropies and ^{14}N-hyperfine interactions.[25,37] Both the CE and TM rely on a three-spin electron-electron-nucleus spin flip process that requires the correct EPR frequency separation, $|\omega_{e2}-\omega_{e1}|=\omega_n$, and an appropriate electron-electron dipolar interaction. These two requirements for the three-spin process suggest new approaches that might be used to improve the efficiency of DNP at high fields (i.e., $\geqslant$5 T).

The use of radical mixtures—50:50 mole % of TEMPO and trityl—to provide EPR spectral intensities matching the required EPR frequency separation, $|\omega_{e2}-\omega_{e1}|=\omega_n$, was shown to yield an improved DNP enhancement relative to that observed using identical concentrations of individual radical species.[38] Furthermore, we recently demonstrated that tethering two TEMPOs to form a biradical polarizing agent is effective in increasing DNP enhancements under high-field cryogenic conditions and has yielded larger enhancements at lower radical concentrations.[27] The improvement in DNP efficiency from using biradicals arises principally from an increased electron-electron dipole coupling and is a consequence of the fixed distance between two TEMPOs. Thus, the modifications of TEMPO biradicals that allow for solubility in aqueous biological media[39] and associated applications[28,32,33,40] have established a new avenue for improving DNP enhanced high-field NMR spectroscopy.

When designing new biradical polarizing agents, it is important to characterize the electron-electron distance and relative orientations of the g tensors between the two tethered radicals. While the contribution of the distance constraint to a biradical in improving its DNP efficiency is obvious, it is *a priori* uncertain whether the molecular linkage between two TEMPOs concurrently constrains the relative g tensors to orientations that lead to the optimal EPR frequency separation. Although the distance between the two electrons may be determined by elegant pulsed EPR techniques involving single[6,41–43] or double[44–48] resonance EPR frequencies, those methods become less effective for short distances and large g anisotropies such as those required for inducing CE or TM. Thus, given that the electron-electron distance required for either CE or TM is usually <25 Å, the appropriate geometry of biradicals suitable for DNP is best determined using continuous-wave (cw) EPR lineshape analyses.[49–52]

This paper describes a series of DNP and EPR experiments with several model biradicals—the bis-TEMPO tethered by n ethylene glycol (BTnE) series that were reported in our previous communication,[27] bis-TEMPO tethered by the urea structure (BTurea), bis-TEMPO tethered by oxalyl amide (BTOXA), and 1-(TEMPO-4-amino)-3-(TEMPO-4-amino)-propan-2-ol (TOTAPOL) (*vide infra*). Microwave driven DNP enhancement profiles were investigated in terms of their dependence on the external magnetic field, irradiation times, radical concentrations, and microwave power. The corresponding DNP efficiency was analyzed in terms of structural data obtained from EPR characterization employing both solution and powder methods. In particular, the constraints of distance and relative g-tensor orientation between the two radicals were determined by solid-state EPR spectra at 9 and 140 GHz and provided insights into the spectral parameters governing the polarization efficiency. We describe a simulation program for powder EPR spectra of biradicals and the parameters that yield the best-fit simulation of the experimental results were refined using a simulated annealing protocol. Thus, the principles for improving DNP enhancements by using biradicals evolve naturally from electron-electron interactions and the EPR frequency separations.

II. THEORETICAL BACKGROUND

A. DNP mechanisms in solid dielectrics

The enhancement ε in nuclear polarization in a DNP experiment is generally defined as

$$\varepsilon = \frac{p}{p_0} - 1, \tag{1}$$

where p and p_0 are the nuclear polarization following microwave irradiation and at thermal equilibrium, respectively. cw microwave-based polarization mechanisms, involving microwave irradiation near ω_e and depending on time-independent hyperfine interactions, include the SE, the CE, and TM which involve single, paired, and multiple electrons, respectively, as the source of electron polarization. The mechanism that best characterizes DNP enhancements is determined by comparing the EPR spectral linewidth δ to the nuclear Larmor frequency ω_n.

When $\delta < \omega_n$, the SE mechanism dominates the microwave driven polarization transfer processes—electron-nuclear transitions that simultaneously flip an electron spin and the coupled nuclear spin.[20] These transitions arise from second-order effects of the nonsecular electron-nuclear dipolar interaction[53] and, consequently, their intensities, as well as the enhancements scale as ω_n^{-2}. When nuclei have $\gamma_n > 0$, where γ_n is the nuclear gyromagnetic ratio, then microwave irradiation at $(\omega_e - \omega_n)$ excites an electron-nuclear transition that results in the maximum positive enhancement, while the transition at $(\omega_e + \omega_n)$ leads to the maximal negative enhancement. The condition $\delta < \omega_n$ allows for separation between the microwave frequencies that generate positive and negative enhancements and hence, avoids cancellation of enhancements from the differing signs. A narrower δ will further optimize the SE enhancements since it increases the efficiency of microwave excitation of the electron-nuclear transitions.

If the EPR spectral breadth and/or linewidth is large, $\delta > \omega_n$, and depending on whether the broadening of the radical's EPR spectrum is inhomogeneous or homogeneous, then either the CE or TM governs the polarization process. In the TM process, the electron-electron dipolar reservoir of a homogeneously broadened EPR lineshape is perturbed by off-resonance excitation of the EPR spectrum,[54] and its nonequilibrium state enhances the nuclear polarization in a collection of three-spin processes. Two electrons and one nucleus are mutually flipped in these three-spin processes, the probability of which is optimized when $\delta \sim \omega_n$.[55] The electron-electron dipolar reservoir is perturbed mainly at the microwave frequencies of $\omega_e - \delta$ and $\omega_e + \delta$, which result, respectively, in the maximum positive or negative enhancement for $\gamma_n > 0$.

In comparison, the CE, which is the dominant polarization considered here, requires two electrons with EPR frequencies, ω_{e1} and ω_{e2}, in an inhomogeneous lineshape and separated by ω_n.[35,56–60] The polarization difference of these two electrons that results from on-resonance microwave excitation can be used to enhance the nuclear polarization, again with a three-spin process. Assuming $\omega_{e1} < \omega_{e2}$ and $\gamma_n > 0$, microwave irradiation at ω_{e1} or ω_{e2} leads to the maximum negative or positive enhancement, respectively. For both TM and the CE, the essential parameters that characterize the three-spin process are the electron-electron interactions, the electron-nuclear interactions, and the correct EPR frequency separation between the two electrons. Specifically, the correct frequency separation, i.e., $|\omega_{e2} - \omega_{e1}| = \omega_n$, yields degenerate spin states involving mutual flips of the spin quantum numbers of the three spins, and the subsequent mixing of the degenerate spin states induces a transition for the desired polarization transfer. In a powder system, the probability of obtaining the correct frequency separation decreases linearly with an increasing EPR spectral breadth that is almost entirely due to g anisotropy in high magnetic fields. Consequently, the enhancement of nuclear polarization from TM and the CE is inversely proportional to the static magnetic field $(1/B_0)$.

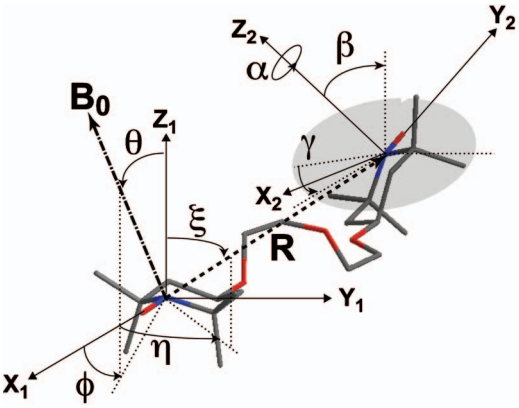

FIG. 1. (Color) An illustration of the relative orientations between the principal axis systems of two tethered TEMPOs ($\mathbf{X}_1\mathbf{Y}_1\mathbf{Z}_1$ and $\mathbf{X}_2\mathbf{Y}_2\mathbf{Z}_2$) of the BT2E biradical (in the skeleton of the heavy atoms), the interelectron vector ($\mathbf{R}$), and the external magnetic field ($\mathbf{B}_0$). The Euler angles (α, β, γ) transform $\mathbf{X}_2\mathbf{Y}_2\mathbf{Z}_2$ into $\mathbf{X}_1\mathbf{Y}_1\mathbf{Z}_1$; $(\eta, \xi, 0)$ and $(\phi, \theta, 0)$ orient $\mathbf{R}$ and $\mathbf{B}_0$, respectively, with respect to $\mathbf{X}_1\mathbf{Y}_1\mathbf{Z}_1$. The Euler angles are listed in the order to rotate the axes along $\mathbf{Z}$, $\mathbf{Y}'$, and $\mathbf{Z}'$ [the convention used by Rose (Ref. 84) and Edmonds (Ref. 63)]. The x axis is along the N–O bond and z axis is perpendicular to the C(NO)C plane and in the π orbital plane (Ref. 50).

B. Powder EPR lineshape of a biradical

For a biradical with an electron-electron distance <25 Å, an analysis of the cw-EPR spectra can be used to determine the distance and relative orientation of the g tensors of the two unpaired electrons.[50] Specifically, the multifrequency EPR lineshape fitting used here employs the known principal values of the g and hyperfine tensors of the monomeric TEMPO-based radical species that comprise the biradical of interest. Further, within the same solvent medium, these principal values are assumed independent of the details of the molecular structures attached to the TEMPO ring, such as a hydroxy (or amino) function group and the various molecular tethers. Simulation of the powder EPR spectrum of a biradical then involves varying the parameters that describe the angles defining the relative orientations of the g tensors $(\mathbf{g}_1, \mathbf{g}_2)$ and hyperfine tensors $(\mathbf{A}_1, \mathbf{A}_2)$ and the interelectron distance $(\mathbf{R})$. This is illustrated in Fig. 1 which shows a schematic model of the BT2E biradical (*vide infra*). Specifically, the Cartesian coordinates are transformed from

the principal axis system (PAS) of the $\mathbf{g}_1$ tensor to the PAS of the $\mathbf{g}_2$ tensor by a rotation matrix, $\mathbf{R}_{21}(\alpha,\beta,\gamma)$, from the PAS of the $\mathbf{g}_1$ tensor to the axis frame with its z axis parallel to $\mathbf{R}$ by $\mathbf{R}_{1D}(\eta,\xi,0)$ and from the PAS of the $\mathbf{g}_1$ tensor to the laboratory frame with its z axis along the external magnetic field $\mathbf{B}_0$ by $\mathbf{R}_{1L}(\phi,\theta,0)$. The zero angle for the third rotation in the above coordinate transformations is a consequence of the axial symmetry of both $\mathbf{R}$ and $\mathbf{B}_0$. Note that for TEMPO-based biradicals, the principal axis systems of the g and hyperfine tensors are coaxial.[61]

Subsequently, the spin Hamiltonian (in Hz) describing a nitroxide biradical is

$$H_0 = (\beta_e B_0 g_1 S_1 - \gamma_n B_0 I_1 + S_1 A_1 I_1) + (\beta_e B_0 g_2 S_2 - \gamma_n B_0 I_2 + S_2 A_2 I_2) + D(3S_{1z}S_{2z} - S_1 S_2) - 2JS_1 S_2, \quad (2)$$

where β_c is the Bohr magneton for the electrons $(\mathbf{S}_1,\mathbf{S}_2)$, γ_n is the gyromagnetic ratio for the coupled nitrogen nuclei $(\mathbf{I}_1,\mathbf{I}_2)$, D is the dipolar interaction between two electrons, and J is the exchange integral from the electron-electron Coulomb interaction.[64] The orientation dependence of $\mathbf{g}_1$, $\mathbf{g}_2$, $\mathbf{A}_1$, and $\mathbf{A}_2$ is calculated from

$$g_1 = R_{1L} g_1^{\mathrm{PAS}} R_{1L}^{-1},$$

$$A_1 = R_{1L} A_1^{\mathrm{PAS}} R_{1L}^{-1},$$

$$g_2 = R_{1L} R_{21} g_2^{\mathrm{PAS}} R_{21}^{-1} R_{1L}^{-1},$$

$$A_2 = R_{1L} R_{21} A_2^{\mathrm{PAS}} R_{21}^{-1} R_{1L}^{-1},$$

where the rotation matrices are constructed in the usual manner[84,63,65] with $\mathbf{R}_{21}(\alpha,\beta,\gamma)$ being

$$R_{21} = \begin{pmatrix} \cos\alpha\cos\beta\cos\gamma - \sin\alpha\sin\gamma & \sin\alpha\cos\beta\cos\gamma + \cos\alpha\sin\gamma & -\sin\beta\cos\gamma \\ -\cos\alpha\cos\beta\sin\gamma - \sin\alpha\cos\gamma & -\sin\alpha\cos\beta\sin\gamma + \cos\alpha\cos\gamma & \sin\beta\sin\gamma \\ \cos\alpha\sin\beta & \sin\alpha\sin\beta & \cos\beta \end{pmatrix}.$$

The g anisotropy of TEMPO is much less than the associated isotropic g value. Thus, in Eq. (2), only g_{1zz} and g_{2zz} are considered, and hence, the angular momenta of the electron spins are quantized along $\mathbf{B}_0$. Omitting the nuclear Zeeman terms (see Appendix A), the Hamiltonian in Eq. (2) is simplified to

$$H = (\beta_e B_0 g_{1zz} S_{1z} + \tilde{A}_{1zz} S_{1z} I'_{1z}) + (\beta_e B_0 g_{2zz} S_{2z} + \tilde{A}_{2zz} S_{2z} I'_{2z}) + D(2S_{1z}S_{2z} - S_{1x}S_{2x} - S_{1y}S_{2y}) - 2J(S_{1z}S_{2z} + S_{1x}S_{2x} + S_{1y}S_{2y}), \quad (3)$$

where the primed nuclear spin operators denote the angular momenta of nuclei that are quantized along their own hyperfine fields that depend on the spin quantum states of the hyperfine-coupled electrons. In the new quantization frames, the coefficients for the hyperfine terms in Eq. (3) are

$$\tilde{A}_{1zz} = \sqrt{nA_1A_1n} = \sqrt{nR_{1L}(A_1^{\mathrm{PAS}})^2 R_{1L}^{-1} n},$$

$$\tilde{A}_{2zz} = \sqrt{nA_2A_2n} = \sqrt{nR_{1L}R_{21}(A_2^{\mathrm{PAS}})^2 R_{21}^{-1}R_{1L}^{-1} n},$$

with

$$n = \begin{pmatrix} 0 \\ 0 \\ 1 \end{pmatrix}.$$

Moreover, the interelectron dipolar interaction D is expanded as

$$D = \frac{\omega_d}{2}(1 - 3\cos^2\mu),$$

where μ is the angle between the directions of $\mathbf{R}$ and $\mathbf{B}_0$ and ω_d is a dipolar coupling constant defined, with $\bar{g}_1 = \frac{1}{3}(g_{1xx} + g_{1yy} + g_{1zz})$ and $\bar{g}_2 = \frac{1}{3}(g_{2xx} + g_{2yy} + g_{2zz})$, as

$$\omega_d \approx \frac{\bar{g}_1 \bar{g}_2 \beta_e^2}{|R|^3},$$

which is about 52.2 GHz/Å^2 between two TEMPOs. In the reference PAS of the g_1 tensor, $\cos(\mu)$ can be evaluated as

$$\cos\mu = nR_{1L}R_{1D}^{-1}n.$$

The matrix representation of Eq. (3) is block-diagonal with $(2I_1+1)(2I_2+1)$ pseudo-two-spin (4×4) blocks labeled by the nuclear spin quanta (m_{I1},m_{I2}). Subsequently, the hyperfine interactions are treated as effective electron Zeeman interactions, which appear in the (m_{I1},m_{I2}) labeled submatrices H^k as

$$H^k = \langle m_{I1}m_{I2}|H|m_{I1}m_{I2}\rangle = (\beta_e B_0 g_{1zz} + m_{I1}\tilde{A}_{1zz})S_{1z} + (\beta_e B_0 g_{2zz} + m_{I2}\tilde{A}_{2zz})S_{2z} + D(2S_{1z}S_{2z} - S_{1x}S_{2x} - S_{1y}S_{2y}) - 2J(2S_{1z}S_{2z} + S_{1x}S_{2x} + S_{1y}S_{2y}). \quad (4)$$

An EPR stick spectrum is calculated from the eigenvalues (λ_i^k) and eigenvectors (Ψ_i^k) of the submatrices in Eq. (4) (see Appendix B). Among the four eigenstates in each submatrix, four allowed EPR transitions are identified as two

transitions from the antiparallel electron spin states (Ψ_2^k, Ψ_3^k) to the highest Zeeman energy parallel spin state (Ψ_1^k) and two transitions from the lowest Zeeman energy parallel electron spin state (Ψ_4^k) to the antiparallel spin states. At a fixed microwave frequency ω_M, the resonance magnetic field for an EPR transition can be calculated from the relationship

$$\frac{\omega_M}{2\pi} = |\lambda_i^k - \lambda_j^k|.$$

For example, based on the result of Appendix B, the resonance magnetic field for the transition $\Psi_2^k \rightarrow \Psi_1^k$ satisfies the self-consistent equation

$$B_{\text{res}}^{L=1,k} = \frac{\frac{\omega_M}{2\pi} - c^k - D + J + \sqrt{(qB_{\text{res}}^{L=1,k} + f^k)^2 + \left(\frac{1}{2}D + J\right)^2}}{p}, \tag{5}$$

where p, q, c^k, and f^k are functions of g_{1zz}, g_{2zz}, $\tilde{A}_{1zz}$, and $\tilde{A}_{2zz}$ and are defined in Appendix B. In practice, $B_{\text{res}}^{L=1,k}$ rapidly converges to an accurate value in the iteration [Eq. (5)] starting from the central field of the EPR spectrum.[50] Further, low-temperature EPR signal intensities (e.g., $P^{L=1,k}$) at the microwave frequency (ω_M) are weighted by the Boltzmann effect as

$$\begin{aligned} P^{L=1,k} &\propto |\langle \Psi_2^k | S_1^+ + S_2^+ | \Psi_1^k \rangle|^2 \exp(-\hbar\omega_M / k_B T) \\ &= (a^k - b^k)^2 \exp(-\hbar\omega_M / k_B T), \end{aligned}$$

$$\begin{aligned} P^{L=2,k} &\propto |\langle \Psi_3^k | S_1^+ + S_2^+ | \Psi_1^k \rangle|^2 \exp(-\hbar\omega_M / k_B T) \\ &= (a^k + b^k)^2 \exp(-\hbar\omega_M / k_B T), \end{aligned}$$

$$P^{L=3,k} \propto |\langle \Psi_4^k | S_1^+ + S_2^+ | \Psi_2^k \rangle|^2 = (a^k - b^k)^2,$$

$$P^{L=4,k} \propto |\langle \Psi_4^k | S_1^+ + S_2^+ | \Psi_3^k \rangle|^2 = (a^k + b^k)^2,$$

where $S_1^+ = S_{1x} + iS_{1y}$, $S_2^+ = S_{2x} + iS_{2y}$, and a^k and b^k are given in Appendix B. When the electron-electron interactions (D and J) shift the energy of antiparallel electron spin states and lead to splittings in the EPR spectrum, low temperatures attenuate one branch of the transitions over the other due to the depleted population difference by $\sim\exp(-\hbar\omega_M / k_B T)$ for the transitions to the higher antiparallel spin state. For single or weakly coupled TEMPO radicals, the altered spin-state populations modify the overall intensity of the signal but do not change the normalized lineshape. However, the lineshape of a biradical with strong electron-electron interactions can change significantly at low temperature.[66] Specifically, the Boltzmann factor leads to significant temperature effects when κ $(\equiv \hbar\omega_M / k_B T)$ reaches 1 and beyond. In discussing 140 GHz EPR spectra at 20 K, this temperature effect is not negligible since $\kappa \sim 0.34$.

Clearly, $B_{\text{res}}^{L=1,k}$ is a function of α, β, γ, η, ξ, R, J, θ, and ϕ. If the biradical molecule is rigid and has only one molecular conformation, α, β, γ, η, ξ, and R are fixed and can be determined from EPR lineshape analyses. However, θ and ϕ are randomly distributed and depend on the orientation of the entire biradical in a powder system. The simulated derivative EPR spectrum $S(B_0)$ is then obtained from the double integral, which we approximate as a double sum over the angles θ and ϕ as

$$S(B_0) = \sum_{L=1}^{4} \sum_{k} \sum_{n=1}^{N_\theta} \sum_{m=1}^{N_\phi} \frac{\sin\theta_n}{N_\theta N_\phi} \frac{-P^{L,k}[B_0 - B_{\text{res}}^{L,k}(\theta_n, \phi_m)]}{\left\{\frac{1}{4}\Gamma^2 + [B_0 - B_{\text{res}}^{L,k}(\theta_n, \phi_m)]^2\right\}^2}, \tag{6}$$

where $\theta = \pi(n - \frac{1}{2})/N_\theta$, $\phi = 2\pi(m-1)/N_\phi$, and Γ is the linewidth for a Lorentzian lineshape.[67] In practice, the exchange integral J is usually small when it involves two electrons with a through space $R > 10$ Å or when the number of covalent σ bonds > 10.[68] Consequently, J is usually excluded from the fitting parameters for biradicals with longer molecular linkages except for the case of the BTurea (*vide infra*) biradical where J is implicated by the biradical structure and manifests itself in the associative solution EPR spectrum.

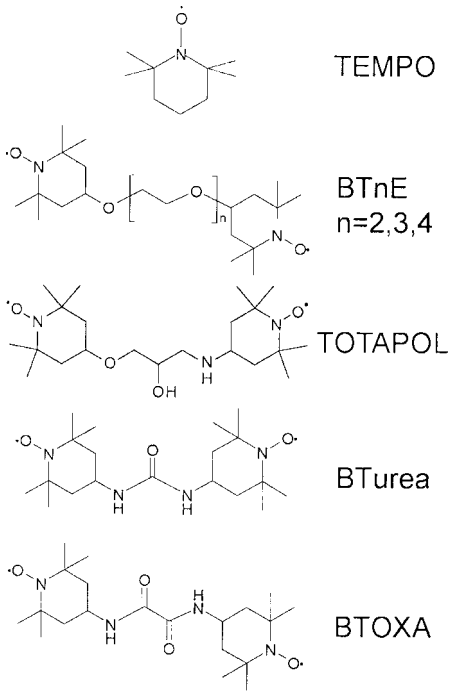

FIG. 2. The structures of TEMPO and six biradicals studied in this paper. In DNP experiments, the TEMPO moieties usually contain natural abundance isotopes. In contrast when recording EPR powder spectra for lineshape analyses, they are ^{15}N and ^{2}H labeled to improve the resolution.

III. MATERIALS AND METHODS

A. Model biradicals

The structures of biradicals investigated in this paper are illustrated in Fig. 2. All reactants used in their preparation were of the highest grades and purchased from Sigma-Aldrich (St. Louis, MO). The biradicals BTnE, bis-TEMPO tethered by n ethylene glycol monomers, where $n=2$, 3, or 4, were synthesized by reacting di-, tri-, or tetraethylene glycol (0.1 mmol) with 4-hydroxy-TEMPO (2,2,6,6-tetramethylpiperidine-1-oxyl-4-ol, 97% free radical, 0.3 mmol) activated by NaH (0.4 mmol) in tetrahydrofuran

(3 ml) under a N_2 atmosphere at 60 °C.[69] The biradical BTOXA, bis-TEMPO tethered by oxalyl amide, was obtained by reacting oxalyl chloride (0.2 mmol) with 4-amino-TEMPO (4-amino-2,2,6,6-tetramethylpiperidine-l-oxyl, 97% free radical, 0.4 mmol) in the presence of triethylamine (1.0 mmol) in toluene (1 ml) at 0 °C. The biradical BTurea, bis-TEMPO tethered by the urea structure, was made by reacting di-imidazole carbonate (0.9 mmol) with 4-amino-TEMPO (1.8 mmol). The biradical TOTAPOL, 1-(TEMPO-4-oxy)-3-(TEMPO-4-amino)-propan-2-ol, was synthesized in two steps.[39] In the first step, 4-hydroxy-TEMPO (60 mmol) was reacted with epichlorohydrin (3.91 ml, 50 mmol) in basic solution (50% w/w NaOH, 10 ml with 0.136 g tetrabutylammonium hydrogensulfate) to obtain 4-(2,3-epoxy-propoxy)-2,2,6,6-tetramethyl-l-piperidinlyoxy [4-(2,3-cpoxy-propoxy)-TEMPO]. A 1.62 g, 7 mmol aliquot of this product was reacted with 4-amino-TEMPO (1.20 g, 7 mmol) in anhydrous CH_3CN (13 ml) with $LiClO_4$ (0.745 mg, 7 mmol) under argon atmosphere overnight at room temperature to obtain TOTAPOL. To provide narrower linewidths in the EPR powder spectra, the TEMPO moieties were ^{15}N, ^{2}H labeled. The isotope labeled 4-hydroxy-TEMPO and 4-amino-TEMPO for the above reactions were purchased from CDN Isotope (Quebec, Canada).

B. DNP experiments

Each DNP sample contained 5 mM biradicals (10 mM electrons) and 2*M* ^{13}C urea in a $^{2}H_6$-DMSO/$^{2}H_2O$/H_2O (60:34:6 w/w/w) mixture that forms a glass at 90 K where the DNP experiments were conducted. The high concentration of ^{13}C urea ensured a more accurate measurement of the NMR signal in the absence of microwaves, and the partial protonation of the solvent was adjusted to maximize the DNP enhancement and the $^{1}H-^{1}H$ spin diffusion process. A sapphire rotor [4 mm outside diameter (OD) from Revolution NMR] was center packed with 25 μl sample solution and maintained at ~90 K for cryogenic MAS-DNP experiments. Each cap stem was grooved and attached to the rotor with cryogenic epoxy (Hysol; Dexter Corporation, Olean, NY) to prevent the drive and sealing caps of the rotor from becoming loose while spinning at low temperature.

DNP-assisted cross polarization magic angle spinning (DNP-CPMAS) experiments were performed on a custom designed, 5 T (140 GHz EPR/211 MHz NMR) system equipped with a superconducting sweep coil (±750 G), a 139.66 GHz/10 W gyrotron microwave source,[29] and a triple channel (e^-, ^{1}H, and ^{13}C) probe capable of performing MAS experiments at ~90 K. The pulse sequence used to acquire the DNP enhanced spectra is illustrated in Fig. 3(a). Initially, the equilibrium Boltzmann ^{1}H polarization is destroyed with a series of 90° pulses, followed by the application of microwave irradiation that generates a buildup of enhanced ^{1}H polarization that is subsequently detected through a standard CPMAS sequence in the presence of two pulse phase modulation (TPPM) decoupling ($\omega_1/2\pi$ =70 kHz for ^{1}H).[70]

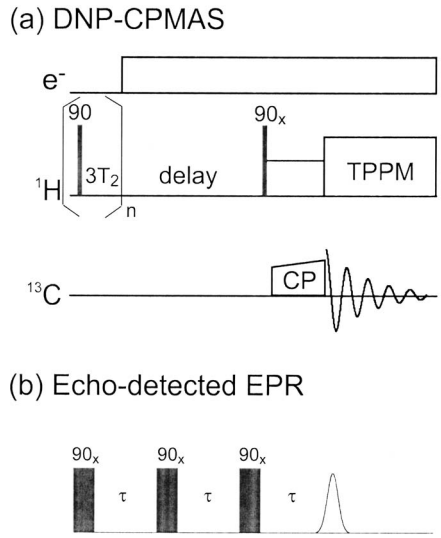

FIG. 3. Pulse sequences for detection of (a) the enhancement of ^{1}H polarization and (b) 140 GHz EPR spectra.

C. Powder EPR spectra at 9 and 140 GHz

Each EPR sample contained 0.5 mM of biradicals (1 mM electrons) in a $^{2}H_6$-DMSO/$^{2}H_2O$ (60:40 w/w) mixture since the removal of environmental ^{1}H spins reduced the EPR linewidth by a factor of about 2. A Bruker EMX spectrometer was used to record 9 GHz cw-EPR spectra at 77 K using a 4 mm quartz tube with an ~60 μl sample immersed in a finger Dewar (WG-819-B-Q; Wilmad LabGlass, Buena, NJ). The spectra measured from progressively diluted biradicals indicated that the residual linewidth was related to the glassy matrix that introduced a distribution of molecular conformations. High-field EPR spectra were recorded with 139.95 GHz microwaves in a 5 T superconducting magnet with a superconducting sweep coil capable of varying the stationary magnetic field by ±4000 G. About a 0.4 μl sample was introduced into a capillary (0.40 inside diameter, 0.55 OD) and placed into a cavity resonator,[71] which was then cooled to 20 K in a cryostat (Oxford Instruments, Oxford, UK). A stimulated-echo pulse sequence, $(\pi/2)_x$-τ-$(\pi/2)_x$-τ-$(\pi/2)_x$-τ-echo with $(\pi/2)_x$=100 ns and τ=200 ns [Fig. 3(b)], was used to detect EPR absorption signals as the magnetic field was swept. The first derivative of the pulsed-echo-detected absorption spectrum approximates the lineshape of the 140 GHz cw-EPR spectrum with a resolution of 1 G.

D. Multifrequency EPR lineshape fitting

The goal of lineshape fitting is to minimize the difference between the simulated EPR powder spectra [S^{sim}, from Eq. (6)] of the biradical and the measured spectra (S^{expt}) at 9 and 140 GHz. Both of the simulated and experimental spectra are normalized and digitized as N data points. The mean square deviation χ^2 is given by

$$\chi^2(\alpha,\beta,\gamma,\eta,\xi,R,J,\Gamma) = \sum_{j=1}^{N} [S_j^{\mathrm{sim}}(\alpha,\beta,\gamma,\eta,\xi,R,J,\Gamma) - S_j^{\mathrm{expt}}]^2.$$

This fitting problem is complex and nonlinear and therefore standard methods that allow a change in the value of the fitting parameters only when the calculated χ^2 is reduced do not necessarily yield a global minimum for χ^2. Therefore, we employed a simulated annealing approach[72–74] that circumvents the problem for the search for a minimum of χ^2 confined near the local minimum. In this manner, the fitting parameters are varied one by one in a sequence and the varied parameters are accepted as the new reference according to Metropolis criteria.[62] The variation is made randomly within a "reasonable" range that is proportional to the "annealing temperature" T_A. When a proposed set of parameters generates a smaller χ^2, it is accepted as the reference for the next trial. However, when the proposed parameter set fails to yield a smaller χ^2, it is not automatically discarded, as is done in standard methods, but is accepted assuming a Boltzmann-type probability defined by the annealing temperature. Specifically, a random number is generated, uniformly distributed between 0 and 1. If it proves to be smaller than $\exp(-\Delta\chi^2/k_BT_A)$, the proposed set of parameters yielding $\Delta\chi^2>0$ is then accepted as the new reference set.

The reasonable range for varying a fitting parameter is selected such that about one-half of the proposed trial parameters are accepted and thus, become actively adjusted within the annealing process. The parameter T_A, which emulates the temperature in the annealing process, is slowly reduced after χ^2 has been calculated for many sets of fitting parameters; these parameters statistically cover the desired range of fitting parameters (the whole range, when T_A is extremely high, and a focused range, when T_A is extremely low). The annealing process can be terminated after an absolute minimum χ^2 is found and the calculated trial χ^2 converges to this minimum. After a simulated annealing process, a further minimization of χ^2 may be achieved using a standard method, e.g., the Nelder-Mead simplex algorithm.[73]

The best-fit parameters for the simulated annealing procedure were determined by incorporating the simulated powder EPR spectra at 9 and 140 GHz via a MATLAB (MathWorks Inc., Natick, MA) environment running on a G4-PowerPC. The range for each set of fitting parameters was varied as described above, i.e., after 20 cycles of sequential changes in these parameters.[75] T_A was then reduced to the 80% level after the range of the varying parameters had been adjusted ten times. In each case, the initial T_A was chosen to keep the associated range of variation reasonable. For the eight variables in the present simulated EPR spectrum, it took about 1 day to explore 20 000 possible sets of fitting parameters. Although the initial set of fitting parameters should be chosen randomly, it can be ascertained roughly from fitting the 140 GHz EPR spectrum for J, R, η, and ξ, given that the splittings that arise from interelectron interactions are better resolved in the 140 GHz spectra. The errors for the refined fitting parameters were estimated according to F statistics by calculating the minimized χ^2 with respect to the remaining parameters as function of the displacement from the optimal value. A conventional bow-shaped curve was fitted by a normal distribution whose standard deviation depicts the fitting error within a canonical level of statistical confidence. For example, two standard deviations represent the accuracy of fitting with 95% confidence.

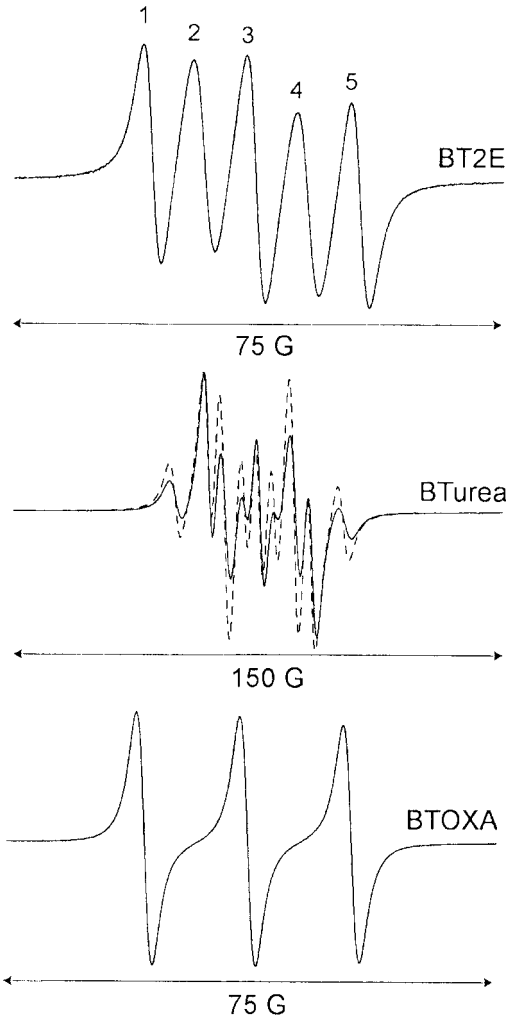

FIG. 4. 9 GHz EPR solution (in ethanol) spectra of biradicals: BT2E, BTurea, and BTOXA. The lineshape of BTurea is approximated by a simulation (dash line) with a time-independent exchange integral $J=\pm 7.7$ G.

IV. RESULTS

A. Solution EPR at 9 GHz

Figure 4 shows the 9 GHz EPR solution spectra of BT2E, BTurea, and BTOXA used to characterize the newly synthesized biradicals. The spectrum of BT2E has two extra lines (2 and 4) in addition to three lines (1, 3, and 5) whose positions coincide with spectral lines of monomeric TEMPO which arise from hyperfine coupling with the ^{14}N ($I=1$), $A_N\sim 15.9$ G. Similar five-peak spectra were observed for BT3E, BT4E, and TOTAPOL, which can be regarded as possessing an average exchange integral (J) much larger than A_N. A time-independent $J\gg A_N$ should result in five-line splitting with a peak intensity ratio $q_2/q_1=2$, where q_1 and q_2 are the intensities of peaks 1 and 2, respectively. However, the transient proximity of the two TEMPOs in BTnE yielded $q_2/q_1<2$ due to a flexible tether.[76] The molecular dynamics involved can be described approximately with a two-state model in which the near proximity of TEMPO moieties leads

to a strong J-coupling constant, while a distant separation results in a negligible J. The temporal fractions of these two states follow the relationships[77]

$$f_n + f_d = 1,$$

$$f_n/f_d = 3(q_2/q_1)/[2 - (q_2/q_1)],$$

where f_n and f_d are the fractions for the near and distant states of a biradical, respectively. The values of f_n/f_d of BT4E, BT3E, BT2E, and TOTAPOL in ethanol are 6.2, 5.5, 5.3, and 0.9, respectively. The absolute lifetimes of these two states cannot be determined by the above analysis but the timescale describing the two-state exchange should be less than A_N^{-1} (i.e., ~20 ns) in order to display an averaged effect of J couplings. As we will see from the simulation below, the flexibility in the tether results in a distribution of molecular conformations of the BTnE series and in TOTAPOL when these biradicals are frozen in a glassy matrix.

In contrast, the rigidity of BTurea and BTOXA biradicals leads to different features in the solution EPR spectra. Figure 4 shows that BTurea exhibits a complex spectrum arising largely from a J coupling comparable to the ^{14}N-hyperfine coupling. The simulated EPR lineshape with a time-independent $J = \pm 7.7$ G yields a good fit of the line frequencies in the solution EPR spectrum of BTurea. This time-independent J coupling, involving either a through-bond or a through-space exchange integral, indicates a short, rigid tether consistent with the computed molecular models. Any discrepancy between the simulation and the experiment may arise from molecular dynamics that perturb the J coupling of BTurea. Figure 4 also shows the spectrum of BTOXA that exhibits an insignificant J coupling due to the rigid tether involved. Although the three-line solution EPR spectrum fails to show in an obvious manner the presence of a biradical, the associated line broadening (~3 G) suggested the proximity of the other paramagnetic moiety in the BTOXA molecule. Despite the smaller number of atoms comprising the BTOXA tether, when compared to the BTnE series, the rigidity of BTOXA's tether keeps the two TEMPOs at a distance and the intensity of the exchange integral becomes negligible. The rigidity of the tethers in both BTurea and BTOXA could constrain the conformation of the biradical in a frozen solution and hence yield relatively well defined relative orientations of g tensors between the two electrons.

B. Powder EPR spectra at 9 and 140 GHz

Multifrequency powder EPR spectra are useful in constraining both the distance and relative g-tensor orientations between two electrons, especially when the distance between the paramagnetic centers is short, as is the case for the biradicals that are potential DNP polarizing agents. These constraints allow the electron-electron dipolar couplings and the EPR frequency separations to be evaluated in order to optimize both the CE and TM polarizing mechanisms. The EPR powder spectra of the TEMPO-based biradicals were recorded in frozen glassy solutions at <100 K. For ^{15}N, ^{2}H labeled TEMPO,[78] the well-known principal values of the g tensor (i.e., $g_{xx}=2.0090$, $g_{yy}=2.0061$, and $g_{zz}=2.0021$) and hyperfine tensor (i.e., $A_{xx}=9.30$ G, $A_{yy}=9.46$ G, and $A_{zz}=51.39$ G) were verified with 9 GHz cw-EPR spectra of 4-hydroxy-TEMPO, 4-amino-TEMPO, and one electron-equivalence reduced biradicals. These principal values also fit the echo-detected 140 GHz EPR spectra, but the agreement with the 140 GHz experimental spectra and simulations is not as good as with the 9 GHz spectra. The reason for this is the more rapid anisotropic relaxation which results in a distortion of the lineshapes in the downfield part of the echo-detected spectra.

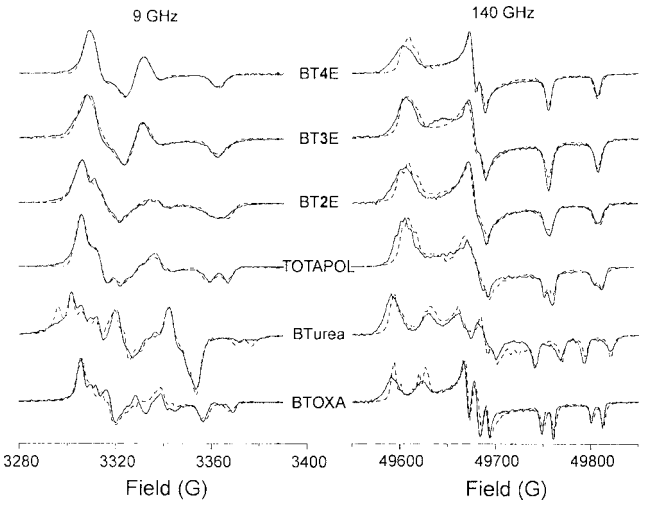

FIG. 5. 9 (*left*) and 140 (*right*) GHz powder EPR spectra (experiments: solid lines; simulations: dash lines) of six biradicals with ^{15}N and ^{2}H labeling. The 9 GHz spectra were recorded at 77 K and the 140 GHz spectra at 20 K. Note that the fitting parameters for BTurea and BTOXA are unique, while simulation of the EPR lineshapes of the BTnE series and TOTAPOL require a distribution of fitting parameters.

Figure 5 illustrates the EPR spectra of the ^{15}N, ^{2}H-labeled biradicals at 9 and 140 GHz with the experimental and simulated spectra depicted as solid and dashed lines, respectively. A qualitative comparison of the 9 and 140 GHz EPR spectra of the flexible BTnE and TOTAPOL biradicals shows that the line broadening is approximately inversely proportional to the number of atoms contained in the tether. The quality of fitting is generally better with the flexible biradical due to the smaller number of splittings, consistent with the larger line broadening parameter Γ used. This broadening effect can be attributed to the multiple conformations of a flexible biradical. In contrast, the visual quality of the fit for both the BTOXA and BTurea spectra deteriorated as these spectra became rich in splittings as a result of electron-electron interactions and a reduction in the distribution of biradical conformations. The specific molecular conformations are consistent with both tethers being in rigid, well defined conformations. As a result, the value of Γ was smaller than that for the flexible biradicals. However, despite the less satisfying visual agreement between the simulations and experimental lineshapes, the fitting parameters, in fact, regressed to smaller errors. That is, the simulated EPR lineshapes for BTurea or BTOXA can be derived from a unique set of parameters, whereas the EPR spectra of the BTnE series and TOTAPOL can be simulated by a distribution of parameters.

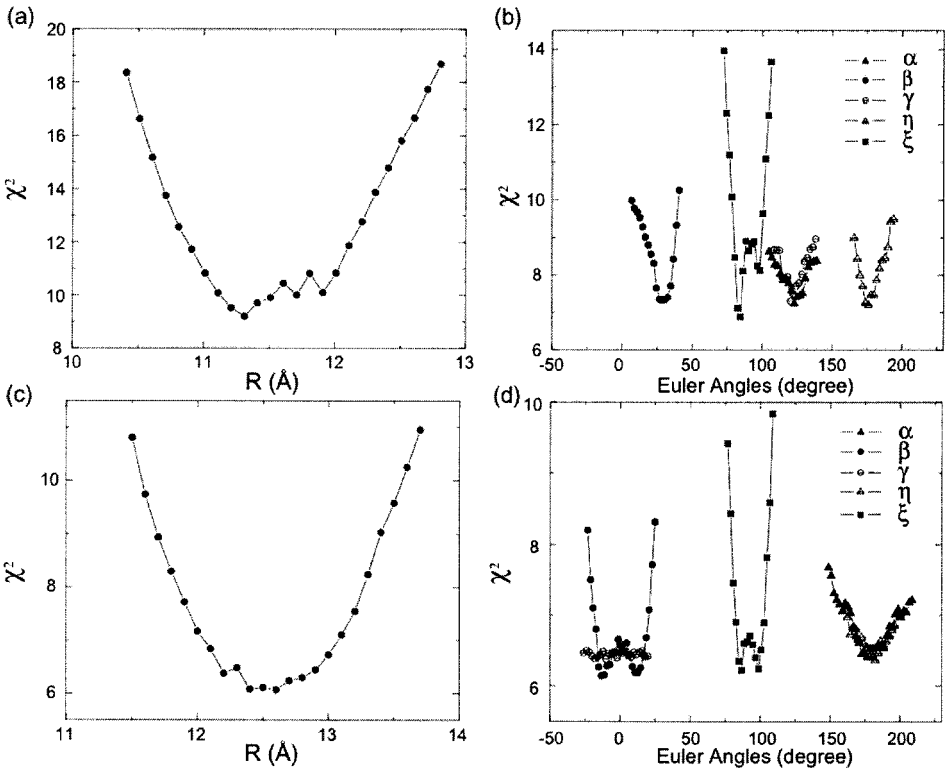

FIG. 6. Fitting errors χ^2 for the distance (R) and Euler angles ($\alpha,\beta,\gamma,\eta,\xi$) in [(a) and (b)] BTurea and [(c) and (d)] BTOXA.

Figure 6 displays the values of χ^2 as a function of the variation in the interelectron distance R and five Euler angles relating the orientation of the two g tensors for BTurea and BTOXA (also a J-coupling constant for BTurea, whose error plot is not shown). Minima in the χ^2 plots strongly constrain the values of the fitting parameters, which provide support for the suggestion that the biradicals exist in a well defined conformation. Note that in the case of BTOXA, the γ angle is not well defined, which is due to the small value of β ($\pm 25°$) which conflates the effect of α and γ on the EPR powder lineshape into that of α. Note that the angles ξ, η, and β are related by a rotation through 90° and the angles α and γ are related by a reflection through 0° (or 180°).[50] The symmetry properties of the angles can be verified when the angles lie close to 0°, 90°, and 180°, as, for example, the ξ and η angles of BTurea and the α, β, γ, ξ, and η angles of BTOXA. In addition, the exact J of $\simeq -7.3$ G simulated for BTurea is consistent with the absolute value from fitting the EPR solution spectrum. That both BTurea and BTOXA have $\xi \sim 90°$ and $\eta \sim 180°$ implies that approximately planar tethers exist in both of these biradicals. Moreover, the planar tether in BTOXA imposes a center of symmetry between the g tensors of tethered TEMPOs, as implied by the angle parameters of $\alpha \sim 180°$, $\beta \sim 0°$, and $\gamma \sim 0°$.

Among the multiple sets of fitting parameters in powder EPR simulations of flexible biradicals such as BTnE and TOTAPOL, the orientation angles are distributed in a broad range and are consistent with the flexibility of the molecular structure. Nevertheless, the distribution of the distance parameter R is relatively narrow and can be treated as an uncertainty corresponding to an averaged distance between the two electrons. Figure 7 shows a slightly different parameter $\Sigma\chi^2$ plotted as a function of the variance of R for each member of the BTnE series and TOTAPOL. To obtain $\Sigma\chi^2$, the fitted χ^2 versus the variation of R is summed over 15 equally well-fitting parameter sets, so that the average electron-electron distance and the associated error are evaluated. Note that distances associated with indistinguishable orientations mentioned previously were only counted once. In general, the average R is close to the optimal value for the minimum $\Sigma\chi^2$. In addition, mapping a Gaussian function onto the $\Sigma\chi^2$ function yields the estimated errors for the derived R. From lineshape simulations, fitting parameters, $\Gamma,\alpha,\beta,\gamma,\xi,\eta,R$, and, specifically for BTurea, J, that best fit the measured EPR spectra are summarized in Table I.

The crystal structure[79] of 4-hydroxy-TEMPO is known as is the relative orientation between the hyperfine and g-tensor principal axes and the geometry of nitroxide radical.[80,81] Thus, the distance and relative g-tensor orientations between two electrons can be converted into atom-atom distances between the atoms of the two

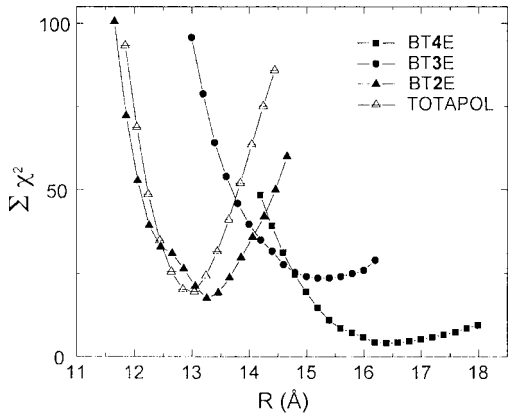

FIG. 7. Fitting errors $\Sigma\chi^2$ for the distances in the BTnE series and TOTAPOL.

TABLE I. Summarized results of fitting parameters for 9 and 140 GHz EPR spectra.

	e^-–e^- distance	Relative orientation of g- and A tensors[a]			e^-–e^-dipole orientation[a]		Exchange integral	Broadening parameter
	R	α	β	γ	ξ	η	J	Γ[b]
Biradical	(Å)	(deg)			(deg)		(G)[c]	(G)[c]
BTurea	11.4±0.2	128	29	120	85	175	−7.3±0.5	2.5
BTOXA	12.6±0.4	182	10	0	88	177	···	2.5
TOTAPOL	13.1±0.6	107	108	124	94	127	···	4
BT2E	13.3±0.8	81	47	16	30	104	···	4
BT3E	15.0±0.8	23	121	297	67	108	···	4
BT4E	16.5±0.9	27	50	211	132	321	···	3

[a]The error associated with the angles is ~±10°. Note that the angle parameters for TOTAPOL and the BTnE series belong to the best-fit among the multiple conformations.
[b]Γ is the full width at half height of a Lorentzian lineshape.
[c]The field unit, G, is converted into frequency unit (Hz) by multiplying $g\beta_e$(~2.807 MHz/G for TEMPO).

moieties of the TEMPOs. These data then serve as input for the structure refinement software CNS (Ref. 82) that leads to the refined structures shown in Fig. 8. The molecular structure databases of the biradicals for CNS were generated by XPLO2D.[83] In the case of BTurea, where the number of atoms in the tether is small, the EPR constraints define the molecular structure to high precision. Much the same is true for BTOXA where we see that the tensors are approximately coaxial. In contrast, the relative orientation of the two TEMPOs in BTnE biradicals is generally not constrained due to the longer molecular linkages involved. Nevertheless, the associated interelectron distance can be described by an average value from a distribution of a more restricted range. Interestingly, although the refined structure of TOTAPOL illustrates a degree of flexibility similar to BT2E, the TEMPO rings are nevertheless constrained to be approximately perpendicular to one another. These two orientations correspond to the g_{yy} and g_{zz} components of the g tensor and yield the EPR frequency separation that is required to satisfy the matching condition for the cross effect polarizing mechanism. Thus, TOTAPOL has both a short distance and the proper orientation of the TEMPO moieties to serve as an effective polarizing agent.

C. Magnetic field dependence of DNP

DNP occurs when microwave radiation of the appropriate frequency excites the EPR transitions of the polarizing agent. Since the gyrotron microwave frequency is presently not tunable, the optimization of the excitation is performed by sweeping the external magnetic field $\mathbf{B}_0$ with a superconducting sweep coil. In top of Fig. 9, we illustrate the 140 GHz EPR spectrum of TEMPO in frozen solution and in the bottom half of the figure the field-dependent profiles of the DNP enhancement obtained from TEMPO and BT2E.

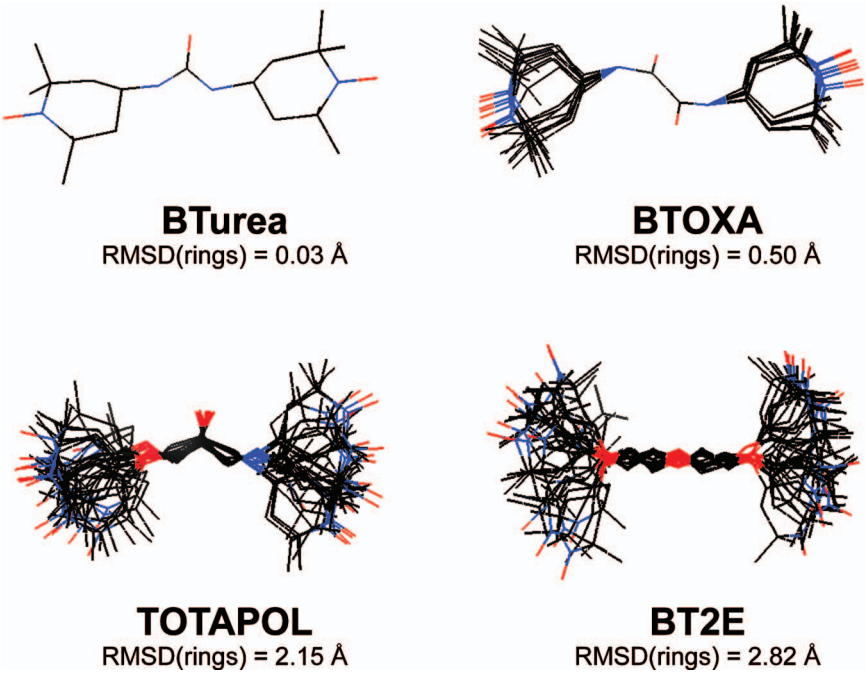

FIG. 8. (Color) The structures of BTurea, BTOXA, TOTAPOL, and BT2E were refined using geometrical constraints obtained from fitting the 9 and 140 GHz EPR lineshapes. The root-mean-square deviations (RMSDs) for the atoms of the TEMPO rings are indicated in the figure.

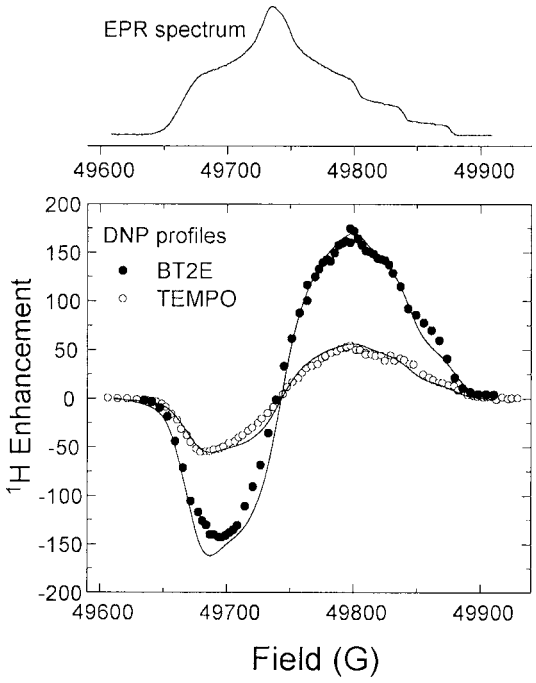

FIG. 9. (Top) The 140 GHz EPR spectrum of TEMPO. (Bottom) Field-dependent ^{1}H DNP enhancement profiles using 5 mM BT2E and 40 mM TEMPO under MAS ($\omega_r/2\pi$=3.5 kHz) at 90 K and 5 T. The smooth lines are for guiding the eyes.

The enhancement profile for TEMPO depends on the probability of finding the correct EPR frequency separation from a randomly oriented TEMPO pair. The TEMPO EPR lineshape (Fig. 9, top) is dominated by g and ^{14}N-hyperfine anisotropies and is an excellent approximation of the EPR spectral density displayed by the BTnE series as well as other biradicals investigated in this paper. In particular, since the dipolar couplings due to the constrained interelectron distance are small (~10–25 MHz) relative to other spectral parameters such as g and hyperfine anisotropies (~600 MHz), they have small effects on EPR absorption lineshape. Note that the 140 GHz EPR spectrum of TEMPO is shifted along the field axis by 58 G in order to align the spectra recorded with the Gunn diode microwave source of the EPR spectrometer (139.95 GHz) with the microwave frequency provided by the gyrotron (139.66 GHz). The optimal magnetic field for DNP is at 49 798 G in Fig. 9 and appears to be ~75 G or ~210 MHz away from the g_{yy} component of the TEMPO lineshape.

The field-dependent profile of the ^{1}H enhancement obtained with 40 mM TEMPO shows a maximum of ~55 at 49 798 G and a minimum of about −55 at 49 783 G, with a zero crossing at 49 735 G corresponding to the g_{yy} component of the EPR absorption. In contrast, the profile from 5 mM BT2E (10 mM electrons) exhibits a similar shape but different intensity from the profile of TEMPO and shows a maximum of ~175 at 49 798 G and a minimum of about −144 at 49 696 G. The larger ^{1}H enhancement observed from BT2E and the changes in the relative position and intensity of the minimum in the negative enhancement are results of the distribution of conformations of the polyethylene glycol tether. Note that the concentrations of TEMPO and BT2E are optimized for the largest DNP enhancement while minimizing the impact of paramagnetic broadening. The similarity in shape of enhancement profiles of 40 mM TEMPO and 5 mM BT2E indicates the central role of electron-electron-nuclear processes involved in both the TM and CE polarizing mechanisms dominating at high and low radical concentrations, respectively.

D. DNP buildup during microwave irradiation

Enhancements in ^{1}H polarization were measured indirectly by transferring ^{1}H polarization from ^{1}H to ^{13}C in a CPMAS experiment. This approach takes advantage of the higher spectral resolution and lower background signal intensities in ^{13}C MAS, as opposed to ^{1}H, spectra. Figure 10(a) illustrates intensity of CP signals of ^{13}C urea following a period of microwave irradiation at the optimal magnetic field position. In contrast, signals without microwave irradiation were much smaller and required long periods of data accumulation in order to be clearly detected. Comparison of DNP enhanced signals with those at thermal equilibrium reflects an enhancement of 172 ± 20 when employing 5 mM BT2E. The enhanced signal grows as the microwave irradiation period increases and displays an exponential behavior defined by

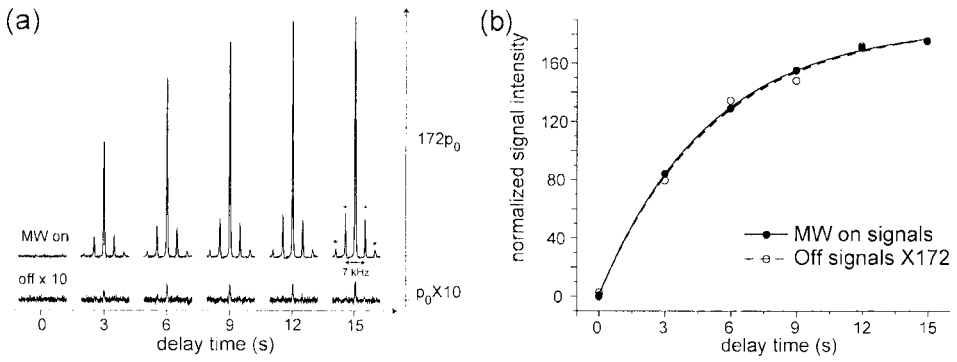

FIG. 10. (a) Buildup of ^{13}C CP signals of ^{13}C urea from the enhanced ^{1}H polarization during a delay of microwave irradiation at the optimal magnetic field position. The ^{1}H enhancement is ~172 by comparing the signals with and without microwaves. (b) The buildup time constant is ~5 s, coinciding with the ^{1}H spin-lattice relaxation time obtained without microwave irradiation. The numbers of acquisitions for enhanced and unenhanced signals are 4 and 32, respectively. The sample, containing 5 mM BT2E biradical, was rotated at a MAS frequency of 3.5 kHz indicated by spinning sidebands (asterisks).

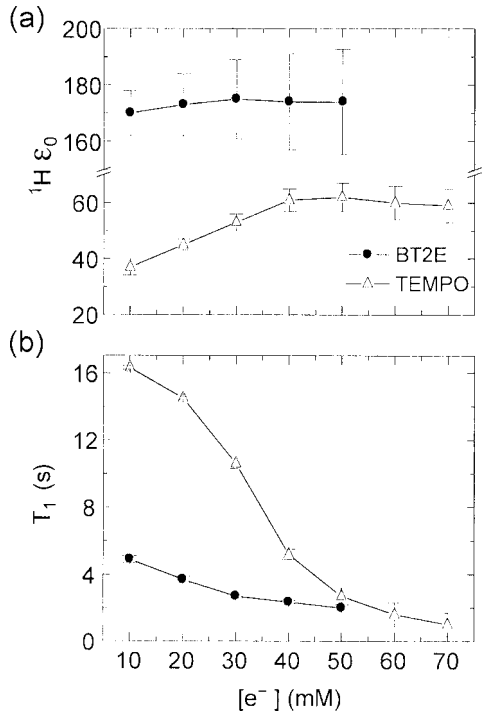

FIG. 11. Radical concentration dependence of (a) DNP enhancement ε_0 and (b) buildup time constant T_1 using BT2E and TEMPO.

$$\varepsilon(t) = \varepsilon_0[1 - \exp(-t/T_1)],$$

where ε is an enhancement factor, t is a delay for microwave irradiation, ε_0 is the equilibrium enhancement, and T_1 is the nuclear spin-lattice relaxation time. Figure 10(b) illustrates the growth in signal intensities following saturation of the ^{1}H polarization with and without microwave irradiation and implies that both the growth of the equilibrium-DNP enhancement and the saturation recovery of the ^{1}H Boltzmann polarization are governed by the same T_1. Empirically, for a given polarizing agent, ε_0 depends on the magnetic field position, the radical concentration, and the microwave power, while T_1 depends only on the radical concentration. The goal in designing polarizing agents is to provide a larger ^{1}H ε_0 and a lower T_1 for the optimal field position, radical concentration, and the available microwave power.

E. Radical concentration dependence of DNP

As long as the DNP enhancement is maintained, a reduction in the radical concentration is desirable since it attenuates electron-nuclear broadening that compromises resolution in the NMR spectra. Figure 11(a) shows that the BT2E biradical yields DNP enhancements that are relatively independent of electron concentrations, while enhancements by the monomeric TEMPO radical are strongly influenced by electron concentrations. BT2E yielded ^{1}H $\varepsilon_0 \sim 175$ at electron concentrations from 10 to 50 mM (multiplied by 0.5 for the biradical concentration), while the ^{1}H ε_0 using TEMPO maximized at ~60 and decreased significantly when the corresponding electron concentration decreased below 40 mM. DNP measurements at higher radical concentration were discounted as the overall enhanced signals decayed due to a reduction in the observable nuclear spins at high radical concentration. The reduction in observable nuclei also led to less intense NMR signals in the absence of microwaves that contributed to larger error bars in measurements of DNP enhancement. Figure 11(b) indicates that the nuclear T_1 depends on the electron concentrations for both BT2E and TEMPO, with the reduction in T_1 being more significant in the case of the TEMPO than that with the BT2E biradical. At higher electron concentrations, this dependence of T_1 tended to converge regardless of whether TEMPO or BT2E was employed.

F. Microwave power dependence of DNP

A strong microwave field is required for efficient DNP, especially when the polarization efficiency decreases in increasing external magnetic fields. When designing polarizing agents, comparisons of DNP efficiency among different biradicals must be made at a controlled level of microwave field strength, which depends on the microwave power and the efficiency of transmission to the sample. However, variations exist in the efficiency with which microwave power is coupled to a sample, and DNP measurements may need to be obtained at different microwave field strengths. To circumvent this issue, one should always investigate the theoretical enhancement at infinite microwave power. This value can be obtained from the microwave power dependence of DNP enhancement described by

$$\frac{1}{\varepsilon_0} = \frac{1}{\varepsilon_{\max}}\left(1 + \frac{1}{aP}\right), \tag{7}$$

where ε_0 is the irradiation time-saturated enhancement, P is the microwave power, $\varepsilon_{\max}$ is the enhancement at infinite microwave power, and a is the saturation parameter, which depends on the microwave transmission efficiency and EPR relaxation properties. Different instrumental conditions affect only a and ε_0 rather than $\varepsilon_{\max}$.

Figure 12 illustrates the relationship between $1/\varepsilon_0$ and $1/P$ for the various biradicals and is depicted in two panels for clarity. The linear plots provide values for $\varepsilon_{\max}$ and a that are summarized in Table II. In addition, we list the DNP enhancements observed using 1.5 W of microwave power, which is the stable power level obtained in long-term experiments, along with the associated T_1 values. The latter were observed to be independent of P since cryogenic MAS circumvented any microwave heating of the sample. The electron-electron distances R from the EPR analyses are listed, as are the corresponding electron-electron dipole coupling constants.

With 10 mM electrons (5 mM biradicals), the trend in the DNP enhancement ε_0 was consistent with the theoretical power-saturated DNP enhancement $\varepsilon_{\max}$, while the ^{1}H relaxation time T_1 remained at about 5–6 s. The value of $\varepsilon_{\max}$ reached a maximum with TOTAPOL and decreased with increasing electron-electron distances in going from BT2E to BT3E and BT4E. The shorter electron-electron distances in BTurea and BTOXA failed to optimize $\varepsilon_{\max}$, with BTOXA yielding insignificant improvement of DNP enhancements ($\varepsilon_0 \sim 50$) notwithstanding the short tether. Despite larger errors associated with the results for the microwave saturation

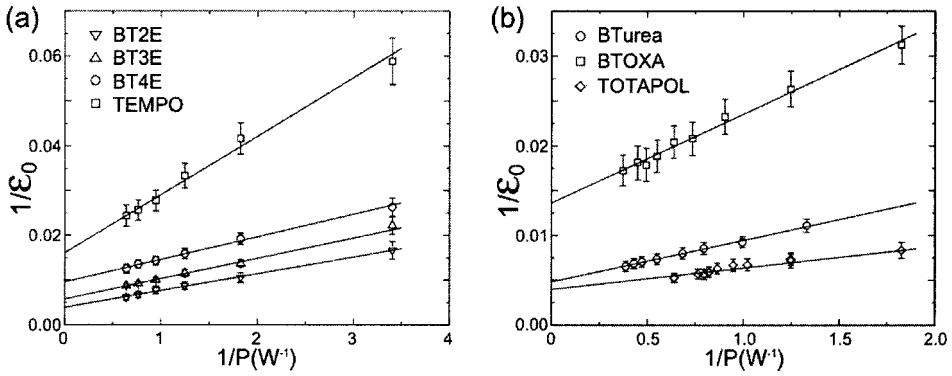

FIG. 12. Microwave power dependence of DNP experiments using (a) the 5 mM BTnE, with $n=2$, 3, and 4, and 10 mM monomeric TEMPO and (b) BTurea, BTOXA, and TOTAPOL, all of which have fewer atoms in their molecular linkers than does BT2E.

parameter a, a trend is clearly present and shows that the close proximity of two electrons required higher microwave power for DNP. Exceptions to this trend occurred with both BTOXA and TEMPO and may be attributable to the unique molecular tether in BTOXA and the possible aggregation of TEMPO.

V. DISCUSSION

DNP experiments using TEMPO-based polarizing agents rely on the CE or TM polarizing mechanisms that dominate at low or high concentrations of the paramagnetic species, respectively, in high magnetic fields. Electron-electron-nucleus three-spin processes involved in both the CE and TM are characterized by an essential electron-electron interaction and a EPR frequency separation that provides the criteria for designing better polarizing agents and optimizing polarization conditions in DNP experiments. Information on the important spectral parameters involved in DNP mechanisms can be ascertained using solution- and solid-state EPR spectroscopies.

The electron-electron dipole coupling that is determined by the electron-electron distance in a biradical depends on the electron concentration when monomeric radicals are used. In general, biradicals yield larger DNP enhancements ($\varepsilon_0 \sim 190$) over shorter polarizing times ($T_1 \sim 5.5$ s) and at lower concentrations ($[e^-] \sim 10$ mM). These improvements, when compared to the results of TEMPO, show dramatic increases in the potential for DNP applications. The BTnE biradicals demonstrate a trend of increasing DNP enhancement with a decrease in intramolecular electron-electron distance. However, in comparing DNP results obtained with TOTAPOL, BTurea, and BTOXA, this trend is not present and, in fact, the largest DNP enhancement was obtained from TOTAPOL, which has a similar R to that of the BT2Es. In addition, the corresponding ε_{max} at infinite microwave power further emphasizes the improved DNP performance of TOTAPOL versus BT2E; this superiority may be attributable to the constrained fixed distance between two electrons in TOTAPOL, which is implied by the solution- and solid-state EPR spectra that reveal the smallest ratio of "near" state to "distant" state in solution spectra. There are also clear features of a dipolar splitting in the solid state lineshapes.

Moreover, although both BTurea and BTOXA have a shorter tether and therefore a smaller R value, they fail to yield a larger ε_0. The theoretical ε_{max} of BTurea falls between that of BT2E and BT3E, indicating that either the electron-electron dipole coupling constant is too strong and increases the electron spin-lattice and spin-spin relaxation rates which interferes with microwave saturation and therefore the DNP process that provides the driving force for both CE and TM mechanisms. BTOXA, which has a smaller R than BT2E, displayed little improvement in DNP efficiency when compared to TEMPO. This result may reflect the shorter relaxation times and the fact that the EPR frequency separation is small because of the coaxiality of the g tensors of the two TEMPO molecules. The features due to the electron dipole splittings that can be clearly observed in the EPR spectra of BTurea and BTOXA provide us with standards to

TABLE II. Summary of ^{1}H DNP measurements from employment of various polarizing agents.

Biradical $[c^-]=10$ mM	Enhancement at 1.5 W[a] ε_0	Buildup time constant T_1 (s)	Enhancement at ∞ power ε_{max}	Saturation factor a (W^{-1})	$e^- - e^-$ distance R (Å)	DCC[b] ω_d (MHz)
TOTAPOL	190 ± 20	5.5 ± 0.2	335 ± 65	0.83 ± 0.30	13.1 ± 0.6	23.2 ± 3.2
BT2E	175 ± 20	4.9 ± 0.2	260 ± 55	1.03 ± 0.40	13.3 ± 0.8	22.2 ± 4.0
BT3E	115 ± 10	5.9 ± 0.2	175 ± 30	1.25 ± 0.35	15.0 ± 0.8	15.5 ± 2.5
BT4E	80 ± 10	6.3 ± 0.2	105 ± 20	1.87 ± 0.35	16.5 ± 0.9	11.6 ± 1.9
BTurea	125 ± 10	5.1 ± 0.2	205 ± 40	1.03 ± 0.40	11.4 ± 0.2	35.2 ± 1.9
BTOXA	50 ± 5	11.3 ± 0.5	70 ± 10	1.37 ± 0.45	12.6 ± 0.4	26.1 ± 2.5
TEMPO	40 ± 5	16.5 ± 0.5	60 ± 15	1.23 ± 0.50	56[c]	0.3

[a]Stable microwave power level employed for extended experiments.
[b]Dipole coupling constant: $\omega_d = 52\,160/R^3$ (MHz) for a TEMPO pair.
[c]The interelectron distance for monomeric TEMPO approximates the average intermolecular distance determined by the radical concentration. At the electron concentration of 10 mM, $\langle R \rangle$ is ~56 Å.

develop our EPR lineshape fitting methodologies. While the unique constraint of *g*-tensor orientation in BTurea does not appear to enhance the DNP efficiency, the constraint in BTOXA does show a significant influence on the DNP enhancement. The EPR powder spectra at 9 and 140 GHz revealed that the relative *g*-tensor orientation in BTOXA is constrained about a center symmetry that suppresses the separation of EPR frequencies, regardless of the orientation of the biradical in the powder distribution. Therefore, the required condition $|\omega_{e2}-\omega_1|=\omega_n$ is not satisfied and the three-spin process is suppressed.

To summarize, the DNP efficiency is optimized by varying the electron-electron distance in the flexible BTnE series and TOTAPOL. In addition, the failure to improve DNP enhancements using rigid BTOXA verifies the importance of the CE mechanism at low electron concentrations, and the absence of EPR frequency separation in the center-symmetric *g*-tensor orientations explains the low enhancements obtained with this biradical.

With a well behaved biradical, the DNP efficiency can be optimized for various experimental conditions, including magnetic field position, irradiation time, biradical concentration, and microwave power. At a constant microwave frequency, a correct magnetic field position allows for EPR saturation that induces the strongest CE enhancement. The net DNP enhancement results from two counteracting CE processes that arise from EPR spectral densities at resonance offsets from the microwave frequency of $\pm\omega_n$, if the associated EPR absorption line is inhomogeneous and broader than ω_n. Given that the electron-electron interactions involved in the selected biradicals are smaller than ω_n (212 MHz for ^{1}H in these experiments), the various EPR spectral profiles yield similar magnetic field-dependent enhancement profiles.

The growth of enhanced nuclear polarization that occurs during the microwave irradiation period and the saturation-recovery process are characterized by nuclear spin-lattice relaxation times T_1. Although the designed biradical polarizing agents allow for efficient polarization transfer from electrons to coupled nuclei, complete polarization of bulk nuclei using diluted paramagnetic species also relies on homonuclear spin diffusion. The rate of nuclear spin diffusion is determined by the average homonuclear dipolar interaction, which can be described by the population density and is potentially affected by the MAS frequency. In the experiments conducted here, the larger DNP enhancements were obtained in glassy matrices that were partially deuterated so that the ^{1}H–^{1}H spin diffusion remained effective during DNP-CPMAS experiments.

A low radical concentration is desirable in DNP applications since the ancillary effect of electron-nuclear relaxation increases NMR linewidths and reduces the number of detectable nuclei close to the radicals. With constrained electron-electron distances, biradicals can yield a DNP enhancement that is independent of electron concentration in contrast to the case of TEMPO where a higher concentration is required to mediate interaction between two electrons. Note that at electron concentrations <10 mM, T_1 becomes impractically long and that ε_0 for the biradicals eventually decreases with a reduction in concentration of the polarizing agent. At electron concentrations higher ($\geqslant 10$ mM) than those typically used in EPR spectroscopy, analysis of $1/\varepsilon_0$ versus $1/C$ (radical concentration) becomes no longer applicable because of unavoidable electron-electron interactions between any two molecules. Instead, the influence of concentration on DNP is determined through the inter-radical distance, density of polarizing centers, and the radical-induced nuclear relaxation. Since a biradical already has the required electron-electron distance, the influences of polarization density and paramagnetic relaxation counteract and lead to an insignificant concentration dependence of DNP with the biradical. The concentration-saturated enhancement also depends on the population density of nuclear spins. The natural abundance of protons in typical samples will empirically reduce the DNP enhancement factor by at least twofold, when compared to the protonation level in deuterated samples.

Microwave irradiation in the CE and TM mechanisms is used to saturate the on-resonance EPR transitions and then to generate polarization differences between the on- and off-resonance electrons. As mentioned previously, the polarization difference is simultaneously transferred to the dipolar coupled nuclei via a three-spin process. The independence of T_1 from the applied microwave power reflects the fact that the nuclear polarization is regulated by the three-spin processes under quasiequilibrium resulting from microwave saturation. Successful saturation of the EPR transitions requires a strong microwave field and long EPR relaxation times. However, microwave saturation can be impeded by a short electron spin-lattice relaxation time, which is required for multiple polarization transfers at diluted electron concentrations and is a consequence of efficient three-spin processes with strong electron-electron interactions. Therefore, strong microwave power is a usual requirement to provide efficient polarization transfers, with any heating arising from microwave irradiation being compensated by the purging gas used for MAS.

Although infinite microwave irradiation power is impractical, the theoretical $\varepsilon_{\max}$ can be derived from the relationship between $1/\varepsilon_0$ and $1/P$ and the saturation parameter obtained, dependent on microwave coupling, relaxation times, and electron concentration. A reasonable comparison of DNP efficiencies among various biradicals can be performed on the basis of ε_0 and a. To date, TOTAPOL yields the largest DNP enhancement of $\sim$190 at 1.5 W in a 4 mm rotor. Its theoretical enhancement $\varepsilon_{\max}\sim 335$ is also the largest and is consistent with a separate measurement made in a 2.5 mm rotor. Furthermore, the associated a [see Eq. (7)] has the smallest value, reflecting a more efficient three-spin process.

VI. CONCLUSIONS

A variety of biradicals having different tethers were analyzed with the goal of improving CE-DNP. Each biradical was characterized by its EPR lineshape, which serves to define the intramolecular electron-electron distance and the relative *g*-tensor orientation between electrons. Excellent agreement between ^{1}H enhancements in the DNP experiments and the parameters used to fit EPR spectra provide

insights into the underlying electron-electron-nucleus processes involving the cross effect and thermal mixing. Powder EPR lineshape simulations can be modified to estimate the probability of a correct EPR frequency separation by a randomly oriented biradical. The nuclear enhancement obtained from the spectral parameters of DNP, i.e., the EPR, NMR, and microwave frequencies, electron-electron and electron-nuclear interactions, electron and nuclear relaxation, and microwave field strength can be calculated theoretically, which allow for semiquantitative explanations of the DNP results and of the EPR characterization by combining the theoretical model of CE with a simulation program developed for biradical powder EPR spectra.

It is possible to establish the optimal distance constraint for the CE between two electrons, but finding a similar constraint involving the relative g-tensor orientations in a biradical composed of two TEMPOs is not straightforward. It is possible, however, to tether two different radicals in such a way as to optimize the required EPR frequency separation for CE. Developments of appropriate new biradicals and the determination of their spatial parameters by EPR lineshape analyses are currently in progress.

APPENDIX A: ABSENCE OF THE ^{15}N ZEEMAN INTERACTION IN 140 GHz EPR SPECTRA

The nuclear (^{15}N) Zeeman interaction in Eq. (2) can be ignored since it is usually much smaller than the associated hyperfine interaction. Although this argument may not be true at a higher magnetic field such as 5 T, there are only a small portion of TEMPO orientations that yield a hyperfine interaction smaller than the nuclear Larmor frequency. For example, small hyperfine interactions occur only when $\mathbf{B}_0$ lies close to the xy plane of the PAS of one TEMPO. Despite the small hyperfine interaction, the resulting forbidden transitions ($\Delta m_S = \pm 1$, $\Delta m_I = \pm 1$) are not easily resolved due to various homogeneous and inhomogeneous broadenings in the EPR spectrum. Thus, ^{15}N Zeeman interactions are ignored in simulations of both 9 and 140 GHz EPR powder spectra.

APPENDIX B: DIAGONALIZATION OF A TWO-PSEUDO-SPIN-$\frac{1}{2}$ 4×4 MATRIX

The submatrix described by Eq. (4) is

$$H^k = \begin{pmatrix} pB_0 + c^k + (1/2)(D-J) & 0 & 0 & 0 \\ 0 & qB_0 + f^k - (1/2)(D-J) & -(1/2)D - J & 0 \\ 0 & -(1/2)D - J & -q_0B_0 - f^k - (1/2)(D-J) & 0 \\ 0 & 0 & 0 & -pB_0 - c^k + (1/2)(D-J) \end{pmatrix},$$

where the basis states are given by

$$\psi_1^k = \left|m_{s1} = +\tfrac{1}{2}, m_{s2} = +\tfrac{1}{2}, m_{I1}, m_{I2}\right\rangle,$$

$$\psi_2^k = \left|m_{s1} = +\tfrac{1}{2}, m_{s2} = -\tfrac{1}{2}, m_{I1}, m_{I2}\right\rangle,$$

$$\psi_3^k = \left|m_{s1} = -\tfrac{1}{2}, m_{s2} = +\tfrac{1}{2}, m_{I1}, m_{I2}\right\rangle,$$

$$\psi_4^k = \left|m_{s1} = -\tfrac{1}{2}, m_{s2} = -\tfrac{1}{2}, m_{I1}, m_{I2}\right\rangle$$

and

$$p = \tfrac{1}{2}\beta_e(g_{1zz} + g_{2zz}),$$

$$q = \tfrac{1}{2}\beta_e(g_{1zz} - g_{2zz}),$$

$$c^k = \tfrac{1}{2}\gamma_e(\tilde{A}_{1zz}m_{I1} + \tilde{A}_{2zz}m_{I2}),$$

$$f^k = \tfrac{1}{2}\gamma_e(\tilde{A}_{1zz}m_{I1} - \tilde{A}_{2zz}m_{I2}).$$

The eigenvalues are

$$\lambda_1^k = pB_0 + c^k + \tfrac{1}{2}(D-J),$$

$$\lambda_2^k = \sqrt{\left(\tfrac{1}{2}D + J\right)^2 + (qB_0 + f^k)^2} - \tfrac{1}{2}(D-J),$$

$$\lambda_3^k = -\sqrt{\left(\tfrac{1}{2}D + J\right)^2 + (qB_0 + f^k)^2} - \tfrac{1}{2}(D-J),$$

$$\lambda_4^k = -pB_0 - c^k + \tfrac{1}{2}(D-J),$$

and the eigenvectors are

$$\Psi_1^k = \psi_1^k,$$

$$\Psi_2^k = a^k\psi_2^k - b^k\psi_3^k,$$

$$\Psi_3^k = b^k\psi_2^k + a^k\psi_3^k,$$

$$\Psi_4^k = \psi_4^k,$$

with

$$a^k = \cos\varphi^k,$$

$$b^k = \sin\varphi^k,$$

$$\tan\varphi^k = \frac{\tfrac{1}{2}D + J}{qB_0 + f^k + \sqrt{\left(\tfrac{1}{2}D + J\right)^2 + (qB_0 + f^k)^2}}.$$

[1] T. Gullion and J. Schaefer, J. Magn. Reson. (1969-1992) **81**, 196 (1989).
[2] A. McDermott, F. Creuzet, M. Levitt, R. Griffin, R. Gebhardt, and J. Lugtenburg, Biophys. J. **57**, A360 (1990).

[3] P. T. Lansbury, P. R. Costa, J. M. Griffiths, E. J. Simon, M. Auger, K. J. Halverson, D. A. Kocisko, Z. S. Hendsch, T. T. Ashburn, R. G. S. Spencer, B. Tidor, and R. G. Griffin, Nat. Struct. Mol. Biol. **2**, 990 (1995).
[4] B. Reif, C. P. Jaroniec, C. M. Rienstra, M. Hohwy, and R. G. Griffin, J. Magn. Reson. **151**, 320 (2001).
[5] C. P. Jaroniec, B. A. Tounge, J. Herzfeld, and R. G. Griffin, J. Am. Chem. Soc. **123**, 3507 (2001).
[6] P. P. Borbat, H. S. McHaourab, and J. H. Freed, J. Am. Chem. Soc. **124**, 5304 (2002).
[7] R. Ramachandran, V. Ladizhansky, V. S. Bajaj, and R. G. Griffin, J. Am. Chem. Soc. **125**, 15623 (2003).
[8] V. Ladizhansky and R. G. Griffin, J. Am. Chem. Soc. **126**, 948 (2004).
[9] C. M. Rienstra, L. Tucker-Kellogg, C. P. Jaroniec, M. Hohwy, B. Reif, M. T. McMahon, B. Tidor, T. Lozano-Perez, and R. G. Griffin, Proc. Natl. Acad. Sci. U.S.A. **99**, 10260 (2002).
[10] M. Hong, J. D. Gross, and R. G. Griffin, J. Phys. Chem. B **101**, 5869 (1997).
[11] M. Hong and R. G. Griffin, Biophys. J. **74**, A296 (1998).
[12] M. Hong,J. D. Gross, W. Hu, and R. G. Griffin, J. Magn. Reson. **135**, 169 (1998).
[13] V. Ladizhansky, C. P. Jaroniec, A. Diehl, H. Oschkinat, and R. G. Griffin, J. Am. Chem. Soc. **125**, 6827 (2003).
[14] A. T. Petkova, M. Baldus, M. Belenky, M. Hong, R. G. Griffin, and J. Herzfeld, J. Magn. Reson. **160**, 1 (2003).
[15] C. P. Jaroniec, C. E. MacPhee, V. S. Bajaj, M. T. McMahon, C. M. Dobson, and R. G. Griffin, Proc. Natl. Acad. Sci. U.S.A. **101**, 711 (2004).
[16] C. P. Jaroniec, C. E. MacPhee, N. S. Astrof, C. M. Dobson, and R. G. Griffin, Proc. Natl. Acad. Sci. U.S.A. **99**, 16748 (2002).
[17] S. G. Zech, A. J. Wand, and A. E. McDermott, J. Am. Chem. Soc. **127**, 8618 (2005).
[18] T. I. Igumenova, A. E. McDermott, K. W. Zilm, R. W. Martin, E. K. Paulson, and A. J. Wand, J. Am. Chem. Soc. **126**, 6720 (2004).
[19] T. I. Igumenova, A. J. Wand, and A. E. McDermott, J. Am. Chem. Soc. **126**, 5323 (2004).
[20] R. A. Wind, M. J. Duijvestijn, C. Vanderlugt, A. Manenschijn, and J. Vriend, Prog. Nucl. Magn. Reson. Spectrosc. **17**, 33 (1985).
[21] D. J. Singel, H. Seidel, R. D. Kendrick, and C. S. Yannoni, J. Magn. Reson. (1969-1992) **81**, 145 (1989).
[22] M. Afeworki, S. Vega, and J. Schaefer, Macromolecules **25**, 4100 (1992).
[23] M. Afeworki and J. Schaefer, Macromolecules **25**, 4092 (1992).
[24] L. R. Becerra, G. J. Gerfen, R. J. Temkin, D. J. Singel, and R. G. Griffin, Phys. Rev. Lett. **71**, 3561 (1993).
[25] G. J. Gerfen, L. R. Becerra, D. A. Hall, R. G. Griffin, R. J. Temkin, and D. J. Singel, J. Chem. Phys. **102**, 9494 (1995).
[26] M. Rosay, J. C. Lansing, K. C. Haddad, W. W. Bachovchin, J. Herzfeld, R. J. Temkin, and R. G. Griffin, J. Am. Chem. Soc. **125**, 13626 (2003).
[27] K.-N. Hu, H.-h. Yu, T. M. Swager, and R. G. Griffin, J. Am. Chem. Soc. **126**, 10844 (2004).
[28] C. G. Joo, K.-N. Hu, J. A. Bryant, and R. G. Griffin, J. Am. Chem. Soc. **128**, 9428 (2006).
[29] C. D. Joye, R. G. Griffin, M. K. Hornstein, K.-N. Hu, K. E. Kreischer, M. Rosay, M. A. Shapiro, J. R. Sirigiri, R. J. Temkin, and P. P. Woskov, *High Power Generation*, special issue of IEEE Trans. Plasma Sci. **34**, 518 (2006).
[30] V. S. Bajaj, C. T. Farrar, I. Mastovsky, J. Vieregg, J. Bryant, B. Elena, K. E. Kreischer, R. J. Temkin, and R. G. Griffin, J. Magn. Reson. **160**, 85 (2003).
[31] M. K. Hornstein, V. S. Bajaj, R. G. Griffin, K. E. Kreischer, I. Mastovsky, M. A. Shapiro, J. R. Sirigiri, and R. J. Temkin, IEEE Trans. Electron Devices **52**, 798 (2005).
[32] M. L. Mak, V. S. Bajaj, M. K. Hornstein, M. Belenky, R. J. Temkin, R. G. Griffin, and J. Herzfeld, Biophys. J. **88**, 506A (2005).
[33] V. S. Bajaj, M. Mak, M. K. Hornstein, M. Belenky, J. Herzfeld, R. J. Temkin, and R. G. Griffin, Biophys. J. **88**, 203A (2005).
[34] D. G. Crabb and W. Meyer, Annu. Rev. Nucl. Part. Sci. **47**, 67 (1997).
[35] V. A. Atsarkin, Sov. Phys. Usp. **21**, 725 (1978).
[36] N. M. Loening, M. Rosay, V. Weis, and R. G. Griffin, J. Am. Chem. Soc. **124**, 8808 (2002).
[37] C. T. Farrar, D. A. Hall, G. J. Gerfen, S. J. Inati, and R. G. Griffin, J. Chem. Phys. **114**, 4922 (2001).
[38] K.-N. Hu, V. S. Bajaj, M. Rosay, and R. G. Griffin, J. Chem. Phys. **126**, 044512 (2007).
[39] C. S. Song, K.-N. Hu, C. G. Joo, T. M. Swager, and R. G. Griffin, J. Am. Chem. Soc. **128**, 11385 (2006).
[40] P. C. A. van der Wel, K.-N. Hu, J. Lewandowski, and R. G. Griffin, J. Am. Chem. Soc. **128**, 10840 (2006).
[41] G. Jeschke, M. Pannier, A. Godt, and H. W. Spiess, Chem. Phys. Lett. **331**, 243 (2000).
[42] S. Saxena and J. H. Freed, Chem. Phys. Lett. **251**, 102 (1996).
[43] Y. Polyhach, A. Godt, C. Bauer, and G. Jeschke, J. Magn. Reson. **185**, 118 (2007).
[44] A. D. Milov, A. B. Ponomarev, and Y. D. Tsvetkov, Chem. Phys. Lett. **110**, 67 (1984).
[45] A. Weber, O. Schiemann, B. Bode, and T. F. Prisner, J. Magn. Reson. **157**, 277 (2002).
[46] R. G. Larsen and D. J. Singel, J. Chem. Phys. **98**, 5134 (1993).
[47] M. Pannier, S. Veit, A. Godt, G. Jeschke, and H. W. Spiess, J. Magn. Reson. **142**, 331 (2000).
[48] G. Jeschke, A. Koch, U. Jonas, and A. Godt, J. Magn. Reson. **155**, 72 (2002).
[49] G. R. Eaton and S. S. Eaton, in *Spin Labeling Theory and Applications*, edited by J. B. Lawrence and R. Jacques (Plenum, New York, 1989), Vol. 8, p. 339.
[50] E. J. Hustedt, A. I. Smirnov, C. F. Laub, C. E. Cobb, and A. H. Beth, Biophys. J. **72**, 1861 (1997).
[51] E. J. Hustedt and A. H. Beth, Annu. Rev. Biophys. Biomol. Struct. **28**, 129 (1999).
[52] E. J. Hustedt, R. A. Stein, L. Sethaphong, S. Brandon, Z. Zhou, and S. C. DeSensi, Biophys. J. **90**, 340 (2006).
[53] C. P. Slichter, *Principles of Magnetic Resonance* (Springer-Verlag, Berlin, 1990), p. 66.
[54] A. Abragam and M. Goldman, *Nuclear Magnetism: Order and Disorder* (Clarendon, Oxford, 1982).
[55] M. Goldman, *Spin Temperature and Nuclear Magnetic Resonance in Solids* (Clarendon, Oxford, 1970).
[56] C. F. Hwang and D. A. Hill, Phys. Rev. Lett. **18**, 110 (1967).
[57] C. F. Hwang and D. A. Hill, Phys. Rev. Lett. **19**, 1011 (1967).
[58] A. V. Kessenikh, V. I. Lushchikov, A. A. Manenkov, and Y. V. Taran, Sov. Phys. Solid State **5**, 321 (1963).
[59] A. V. Kessenikh, A. A. Manenkov, and G. I. Pyatnitskii, Sov. Phys. Solid State **6**, 641 (1964).
[60] D. S. Wollan, Phys. Rev. B **13**, 3671 (1976).
[61] A. Capiomon, H. Lemaire, B. Chion, and J. Lajzerowicz-Bonneteau, J. Chem. Phys. **60**, 2530 (1974).
[62] N. A. Metropolis, A. Rosenbluth, M. Rosenbluth, A. Teller, and E. Teller, J. Chem. Phys. **21**, 1087 (1953).
[63] A. R. Edmonds, *Angular Momentum in Quantum Mechanics* (Princeton University Press, Princeton, NJ, 1974).
[64] C. W. Chen, *Magnetism and Metallurgy of Soft Magnetic Materials* (Dover, New York, 1986).
[65] D. M. Brink and G. R. Satchler, *Angular Momentum* (Clarendon, Oxford, 1979).
[66] R. Calvo, E. C. Abresch, R. Bittl, G. Feher, W. Hofbauer, R. A. Isaacson, W. Lubitz, M. Y. Okamura, and M. L. Paddock, J. Am. Chem. Soc. **122**, 7327 (2000).
[67] C. P. J. Poole, *Electron Spin Resonance: A Comprehensive Treatise on Experimental Techniques* (Wiley, New York, 1983).
[68] G. R. Luckhurst, in *Spin Labeling Theory and Applications*, edited by L. J. Berliner (Academic, New York, 1976), p. 133.
[69] G. Gagnaire, A. Jeunet, and J. L. Pierre, Tetrahedron Lett. **30**, 6507 (1989).
[70] A. E. Bennett, C. M. Rienstra, M. Auger, K. V. Lakshmi, and R. G. Griffin, J. Chem. Phys. **103**, 6951 (1995).
[71] V. Weis, M. Bennati, M. Rosay, J. A. Bryant, and R. G. Griffin, J. Magn. Reson. **140**, 293 (1999).
[72] S. Kirkpatrick, C. D. Gelatt, and M. P. Vecchi, Science **220**, 671 (1983).
[73] W. H. Press, S. A. Teukolsky, W. T. Vetterling, and B. P. Flannery, *Numerical Recipes in FORTRAN: The Art of Scientific Computing* (Cambridge University Press, New York, 1992).
[74] E. J. Hustedt, C. E. Cobb, A. H. Beth, and J. M. Beechem, Biophys. J. **64**, 614 (1993).
[75] W. L. Goffe, G. D. Ferrier, and J. Rogers, J. Econometr. **60**, 65 (1994).
[76] V. N. Parmon, A. I. Kokorin, G. M. Zhidomirov, and K. I. Zamaraev,

Mol. Phys. **30**, 695 (1975).
[77] N. J. Turro, I. V. Khudyakov, S. H. Bossmann, and D. W. Dwyer, J. Phys. Chem. **97**, 1138 (1993).
[78] W. Snipes, J. Cupp, G. Cohn, and A. Keith, Biophys. J. **14**, 20 (1974).
[79] L. J. Berliner, Acta Crystallogr., Sect. B: Struct. Crystallogr. Cryst. Chem. **26**, 1198 (1970).
[80] R. Improta, K. N. Kudin, G. E. Scuseria, and V. Barone, J. Am. Chem. Soc. **124**, 113 (2002).
[81] G. Jeschke and H. W. Spiess, Chem. Phys. Lett. **293**, 9 (1998).
[82] A. T. Brunger, P. D. Adams, G. M. Clore, W. L. DeLano, P. Gros, R. W. Grosse-Kunstleve, J. S. Jiang, J. Kuszewski, M. Nilges, N. S. Pannu, R. J. Read, L. M. Rice, T. Simonson, and G. L. Warren, Acta Crystallogr., Sect. D: Biol. Crystallogr. **54**, 905 (1998).
[83] G. J. Kleywegt and T. A. Jones, Methods Enzymol. **277**, 208 (199)
[84] M. E. Rose, *Elementary Theory of Angular Momentum* (Wiley, New York, 1957).